

## Article

# A Study of the Laser-Assisted Alloying Effect on Plasmonic Properties of Au-Pd Nanostructured Film Using Surface-Enhanced Raman Spectroscopy

Chawki Awada <sup>1,\*</sup>  and Francesco Ruffino <sup>2,\*</sup> <sup>1</sup> Department of Physics, College of Science, King Faisal University, P.O. Box 400, Al-Ahsa 31982, Saudi Arabia<sup>2</sup> Dipartimento di Fisica e Astronomia "Ettore Majorana", Università di Catania and CNR-IMM, Catania (University) Unit, 95123 Catania, Italy

\* Correspondence: cawada@kfu.edu.sa (C.A.); francesco.ruffino@ct.infn.it (F.R.)

**Abstract:** In this work, we report a study on the effect of the laser-assisted alloying effect on plasmonic properties of Pd and Au-Pd nanostructures using surface-enhanced Raman spectroscopy (SERS). The monometallic and bimetallic nanostructures are formed by nanosecond-laser induced de-wetting and the alloying of pure Pd and bimetallic Au-Pd nanoscale-thick films deposited on a transparent and conductive substrate. The morphological characteristics of the nanostructures were changed by controlling the laser fluence. Then, 4-nitrothiophenol (4-NTP) was used as an adsorbed molecule on the surface of the nanostructures to analyze the resulting SERS properties. A quantitative analysis was reported using the SERS profile properties, such as FWHM, amplitude, and Raman peak position variation. An excellent correlation between the variation of SERS properties and the nanostructures' size was confirmed. The optical enhancement factor was estimated for Pd and Au-Pd nanostructures for the laser fluence (0, 0.5, 0.75, 1, and 1.5 J/cm<sup>2</sup>).

**Keywords:** plasmonic nanostructures; Pd; Au-Pd; bimetallic; SERS; laser

**Citation:** Awada, C.; Ruffino, F. A Study of the Laser-Assisted Alloying Effect on Plasmonic Properties of Au-Pd Nanostructured Film Using Surface-Enhanced Raman Spectroscopy. *Coatings* **2023**, *13*, 797. <https://doi.org/10.3390/coatings13040797>

Academic Editors: Marcin Pisarek and Michał Kulka

Received: 15 March 2023

Revised: 2 April 2023

Accepted: 17 April 2023

Published: 19 April 2023



**Copyright:** © 2023 by the authors. Licensee MDPI, Basel, Switzerland. This article is an open access article distributed under the terms and conditions of the Creative Commons Attribution (CC BY) license (<https://creativecommons.org/licenses/by/4.0/>).

## 1. Introduction

Bimetallic nanostructures have attracted a lot of attention due to their plasmonic and catalytic properties [1–3]. Bimetallic nanostructures have opened the way for various application in catalysis, sensing, renewable energy, environment, biomedicine, medicine, electronics, and food [1–6]. Gold–Palladium (Au-Pd) nanostructures have proved to be a better catalyst than monometallic mixtures of Pd and Au nanoparticles [7]. Au-Pd NPs have been shown to be an excellent catalyst in the colorimetric sensing of hydrazine [8]. Au-Pd colloids were used as surface-enhanced Raman scattering substrates [1].

Selectivity and sensitivity can be improved and tuned by controlling the size and composition of Au-Pd nanostructures [3,9]. Localized surface plasmon resonance (LSPRs) played a crucial role in the mechanism of surface enhanced Raman spectroscopy (SERS) towards the amplification of the detection of the finger print of analyte adsorbed to Au-Pd nanostructures. Confining the local electric field to specific sites with a controllable shape and size is crucial to enhancing the Raman scattering generated by the adsorbed molecules. SERS is a very sensitive vibrational technique for revealing the chemical and structural properties of molecules adsorbed into Au-Pd nanostructures. SERS has been proved to detect sub-monolayers, and even single molecules [10–13].

Different methods have been developed to synthesize bimetallic Au-Pd nanostructures, such as chemical reduction, photoreduction, hydrolysis, microwave-assisted synthesis, thermolysis, and sol-gel synthesis [14–18]. Although the aforementioned chemical routes are cost effective and simple to use, they present some environmental safety limitations due to the presence of chemicals reducing agents and surfactants in their products. Therefore, developing new physical methods to fabricate the bimetallic alloy using pulsed laser is great

of interest for a large application of products. The novelty of this work consists of using new physical methods of fabrication on solid film and using SERS to study and understand the effect of laser fluence on the plasmonic properties of Pd and Au-Pd nanostructures.

## 2. Materials and Methods

### 2.1. Materials Preparation

Slides of glass (soda lime) with a thick Fluorine-doped Tin Oxide ( $\text{SnO}_2\text{:F}$ , FTO) film sputter-deposited on the surface were used (KINTEC, Hung Hom, Kowloon, Hong Kong [19], with an average transmittance of 73.2% in the 400–1100 nm wavelength range, 8.6 ohm/sq sheet resistivity). Pure Pd and bimetallic Au-Pd thin films were deposited on the FTO surface by using an RF Emitech K550X sputter coater (Quorum Technologies, East Sussex, UK). Pd monometallic or Au-Pd bimetallic targets were used, respectively (99.999% purity,  $\text{Au}_{64}\text{Pd}_{36}$  with 64 atomic % Au and 36 atomic % Pd). The effective thickness  $d$  of the deposited metal films was tuned by controlling the deposition time and the emission current, and checked *ex situ* by means of Rutherford backscattering spectrometry analysis (using 2-MeV  $^4\text{He}^+$  incident ions and backscattered at  $165^\circ$ ). In particular, the samples analyzed in this work are characterized by Pd film of thickness  $d_{\text{Pd}} = 17.6$  nm, and a Au-Pd film of thickness  $d_{\text{Au-Pd}} = 48.6$  nm (5% error). The 48.6 nm thickness for the Au-Pd film was chosen so that 36% (as established in the  $\text{Au}_{64}\text{Pd}_{36}$  alloy) of this thickness corresponds to 17.5 nm, the thickness of the sole Pd film.

The metal films on the surface of the FTO/glass slides were irradiated by nanosecond pulsed laser (one pulse per film) exploiting a nanosecond pulsed (12 ns) Nd: yttrium aluminum garnet YAG laser at wavelength of 532 nm (Quanta-ray PRO-Series pulsed Nd:YAG laser, Spectra Physics, Santa Clara, CA, USA). The laser spot was circular with a diameter of approximately 4 mm, and the intensity had a Gaussian spatial distribution (full width at half maximum of 1 mm). For the experiments presented in this work, the peak intensities of 0.50, 0.75, 1.0 and 1.5 J/cm<sup>2</sup> were used (measurement error of 0.025 J/cm<sup>2</sup>). In this experiment the laser beam fell directly onto the sample surfaces with a 4 mm beam diameter (without using focusing lens). However, due to the Gaussian shape of the laser intensity, 97% of the highest laser intensity (peak intensity) was maintained within a circular area of 600  $\mu\text{m}$  in diameter centered at the maximum of laser intensity. Hence, the 4 mm diameter circular area of the film was covered at a single pulse, and the  $M^2$  value for the laser was  $\sim 20$ .

These irradiations served to form Pd or Au-Pd nanoparticles (by a molten-phase de-wetting process [20]) on the FTO surface from the deposited continuous films. However, the Gaussian spatial distribution of the laser intensity determined a decreasing laser intensity from the center to the edge of the circular spot, resulting in different nanostructuring effects. Hence, the data presented in the following refer to the circular area with a diameter of 600  $\mu\text{m}$  from the center of the laser spot [21].

A solution of 4-NTP in ethanol absolute with a concentration of  $10^{-3}$  M was used to functionalize the Pd/FTO and Au-Pd/FTO films. In order to assure a complete bonding between 4-NTP molecules and Pd and Au-Pd atoms towards the thiol group, we immersed the substrate for 24 h. The ethanol was used again in order to eliminate the non-bonded molecules from the substrate that will be used for SERS measurements.

FTO was chosen as the supporting substrate for several reasons:

- (a) It is transparent to the laser wavelength. Hence, it should not be affected by absorbed laser irradiations (at least, at not-so-high laser fluences) and the samples' modifications should be related only to the laser-induced modifications of the metallic films.
- (b) The FTO is also a material with high electrical and thermal conductivity. Hence, during the laser irradiations of the metallic films, the laser-generated heat in the metallic films (by laser energy absorption) can be rapidly dissipated through the conductive substrate, apart very high laser fluences.
- (c) FTO is a transparent and conductive substrate used in several technological applications and plasmonic metallic nanoparticles/FTO systems. Thanks to the combined

optical properties of the nanoparticles, high transparency and high conductivity of the substrate, it can be used in technological applications such as optical sensing, plasmonic solar cells, etc.

## 2.2. Experimental Methods

Scanning electron microscopies (SEM) were performed by using a Zeiss FEG-SEM Supra 25 Microscope (Carl Zeiss Microscopy, New York, NY, USA), and the resulting images were studied by means of Gatan Digital Micrograph software (version 3.0, GATAN Inc., Pleasanton, CA, USA).

The surface roughness (Root Mean Square, RMS) of the samples was evaluated by analyzing Atomic Force Microscopy (AFM) images acquired by using a Bruker-Innova microscope (Bruker Instruments, Billerica, MA, USA) operating in contact mode. Si tips were used to perform these analyses (MSNL-10 from Bruker Instruments, radius of curvature  $\sim 2$  nm). The AFM images were analyzed by means of the SPMLabAnalyses V7.00 software (Veeco Instruments Inc., Plainview, NY, USA).

A confocal Raman spectrometer (LabRAM HR800, Horiba Scientific, Villeneuve-D'Ascq, France) was used to measure the Raman spectra in a backscattering configuration.

The samples were irradiated by a He-Ne Laser with a wavelength of 632.8 nm and an output power of 2 mW. A  $50\times$  objective with a 0.5 numerical aperture and a 1800 L/mm grating were selected for the SERS measurement.

## 3. Results

### 3.1. Morphological Analyses

Figure 1 shows the representative SEM microscopies of the bare FTO surface (a) and of the FTO surface covered with the 17.6-nm-thick Pd film (b) and by the 48.6-nm-thick Au-Pd film (c).

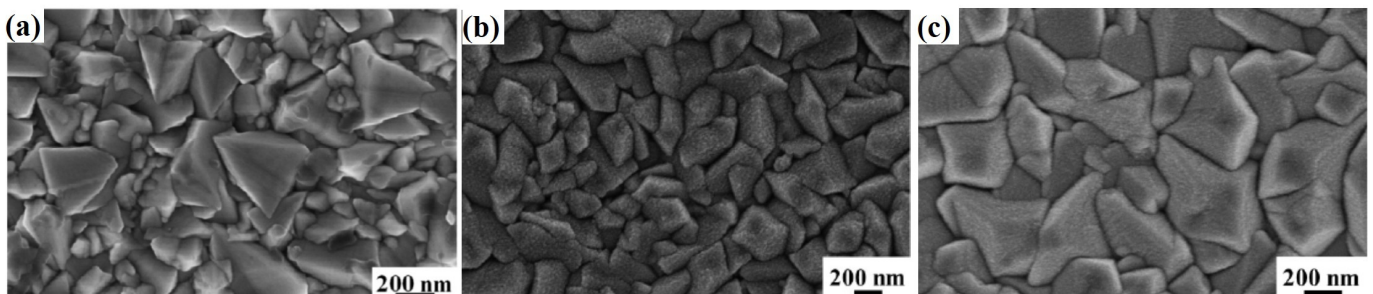


**Figure 1.** SEM images of bare FTO surface (a) and of the FTO surface covered with the 17.6-nm-thick Pd film (b) and by the 48.6-nm-thick Au-Pd film (c).

We can recognize the non-flat topography of the FTO layer on the glass supporting substrate. In fact, by the inspection of the plan-view SEM images, the FTO layer shows a morphology as composed by micrometric structures, randomly located over the entire glass surface, having an approximately truncated pyramidal shape. However, this is the standard morphology for sputter-deposited FTO layers [22] growing by anisotropic columnar structures. After the Pd and Au-Pd depositions, the pyramidal structuration of the FTO layer is still recognizable; however, over the pyramids' surfaces a nano-granular morphology develops, typical for sputtered metal films on non-metal surfaces and arising from the nucleation and growth processes of the metals [23]. By using the SEM images, the mean distance between two neighboring apices of the FTO pyramids was about 220 nm before and after the Au and Au-Pd films' deposition. Similarly, the surface roughness, evaluated by the RMS parameter, was 19.4 nm for the bare FTO and it was the same after the Au and Au-Pd films deposition. These facts indicate that the Au and Au-Pd films, for the effective thicknesses used, conformally covered the FTO surface, following the FTO surface morphology and adapting on the surface without altering the surface planar

distances between apexes of neighboring FTO pyramids and without altering the vertical distances between the highest and lowest points on the surface. Eventually, much higher films thicknesses are required to completely fill the holes between FTO pyramids and to completely cover the FTO surface for a flat, uniform surface. However, this is not of interest for the present results.

Figure 2 shows SEM microscopies of the 17.6-nm-thick Pd film on the FTO surface after laser irradiation at fluence values of  $0.5 \text{ J/cm}^2$  (a),  $0.75 \text{ J/cm}^2$  (b),  $1.0 \text{ J/cm}^2$  (c) and  $1.5 \text{ J/cm}^2$  (d). Similarly, Figure 3 shows representative SEM images of the 48.6-nm-thick Au-Pd film on the FTO surface followed by laser treatment at fluence values of  $0.5 \text{ J/cm}^2$  (a),  $0.75 \text{ J/cm}^2$  (b),  $1.0 \text{ J/cm}^2$  (c) and  $1.5 \text{ J/cm}^2$  (d). In general, metal thin films such as Au and Pd de-wet from the substrate surface during nanosecond-pulsed laser irradiations. The irradiations result in the metallic films melting, followed by holes being formed in the films (reaching the substrate surface) and films retreating away from the holes towards the formation of droplets of a circular section. At the higher fluence values, the vaporization and recondensation of the droplets can also occur [24,25].

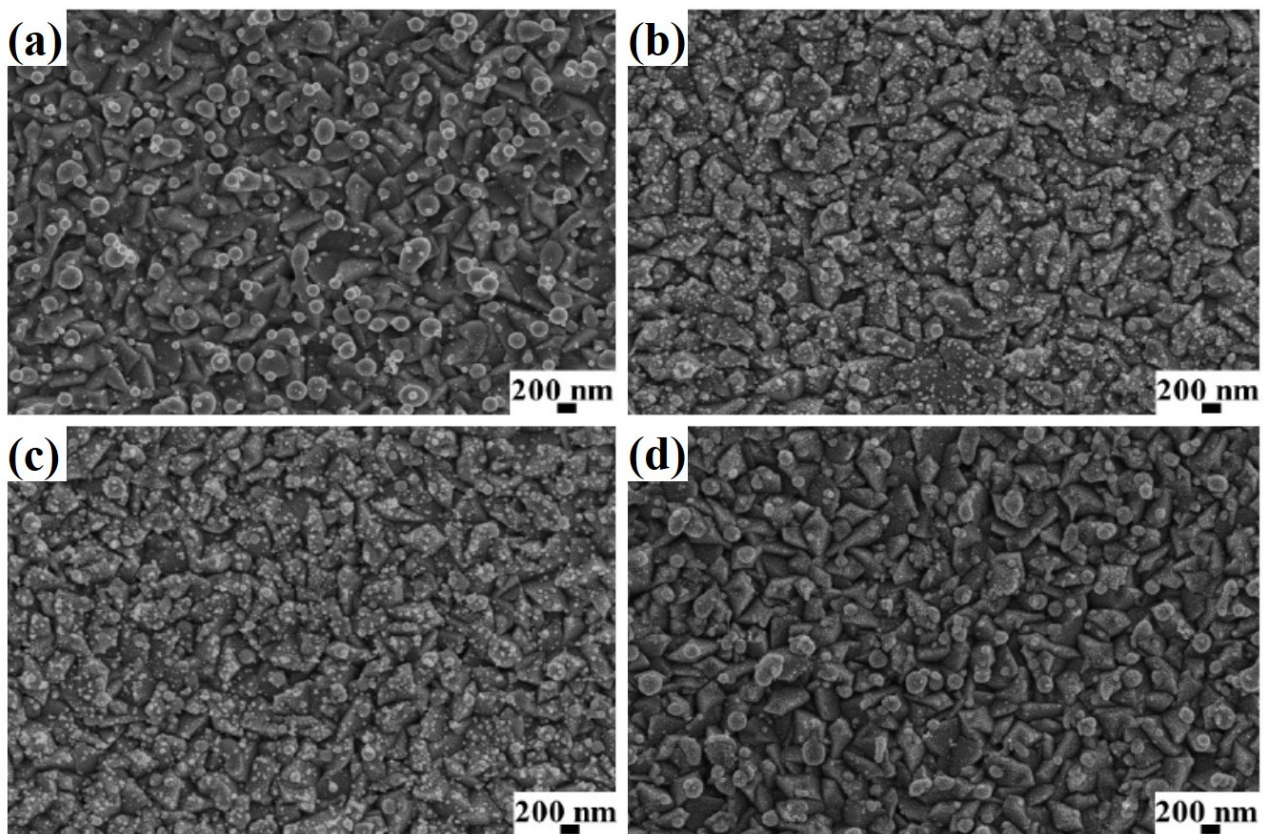


**Figure 2.** SEM images of FTO surface covered by 17.6- nm-thick Pd film and laser irradiated at the fluence values (a)  $0.50 \text{ J/cm}^2$ , (b)  $0.75 \text{ J/cm}^2$ , (c)  $1.00 \text{ J/cm}^2$  and (d)  $1.50 \text{ J/cm}^2$ .

Through the inspection of the SEM images in Figures 2 and 3 we can conclude that the laser irradiations led to the formation of spherical particles, and when the starting thickness of the deposited metal film was fixed, by increasing the laser fluence, a strong modification of the nanoparticles occurred. In general, by increasing the laser fluence, the de-wetting process evolves, leading to more and more separated droplets: at low fluences the film can be only partially de-wetted, i.e., a continuous film is obtained with holes developing along it. By increasing the fluence, the holes grow in planar size, leading to more and more film agglomeration in droplets until a sharp separation is observed between droplets. This is clear from Figure 2a,b and Figure 3a,b. After irradiations at  $0.50 \text{ J/cm}^2$ , droplets with a diameter generally in the 100–200 nm range were obtained in

the case of the 17.6-nm-thick Pd film; droplets with a diameter in the 200–400 nm range were obtained in the case of the 48.6-nm-thick Au-Pd film. These particles were well-separated from each other (high surface–surface gap). The evaluation of the sizes of the de-wetted nanostructures was performed by using the SEM images analyzed by means of the GATAN software; in particular, considering an SEM image, we established a threshold for the brightness of the image resulting in bright areas in the images with intensity value 1 representing the metal particles, and in dark areas with intensity value 0 representing the supporting substrate. The size  $D$  of a particle was evaluated as the diameter of the smaller circumference inscribing the particle.

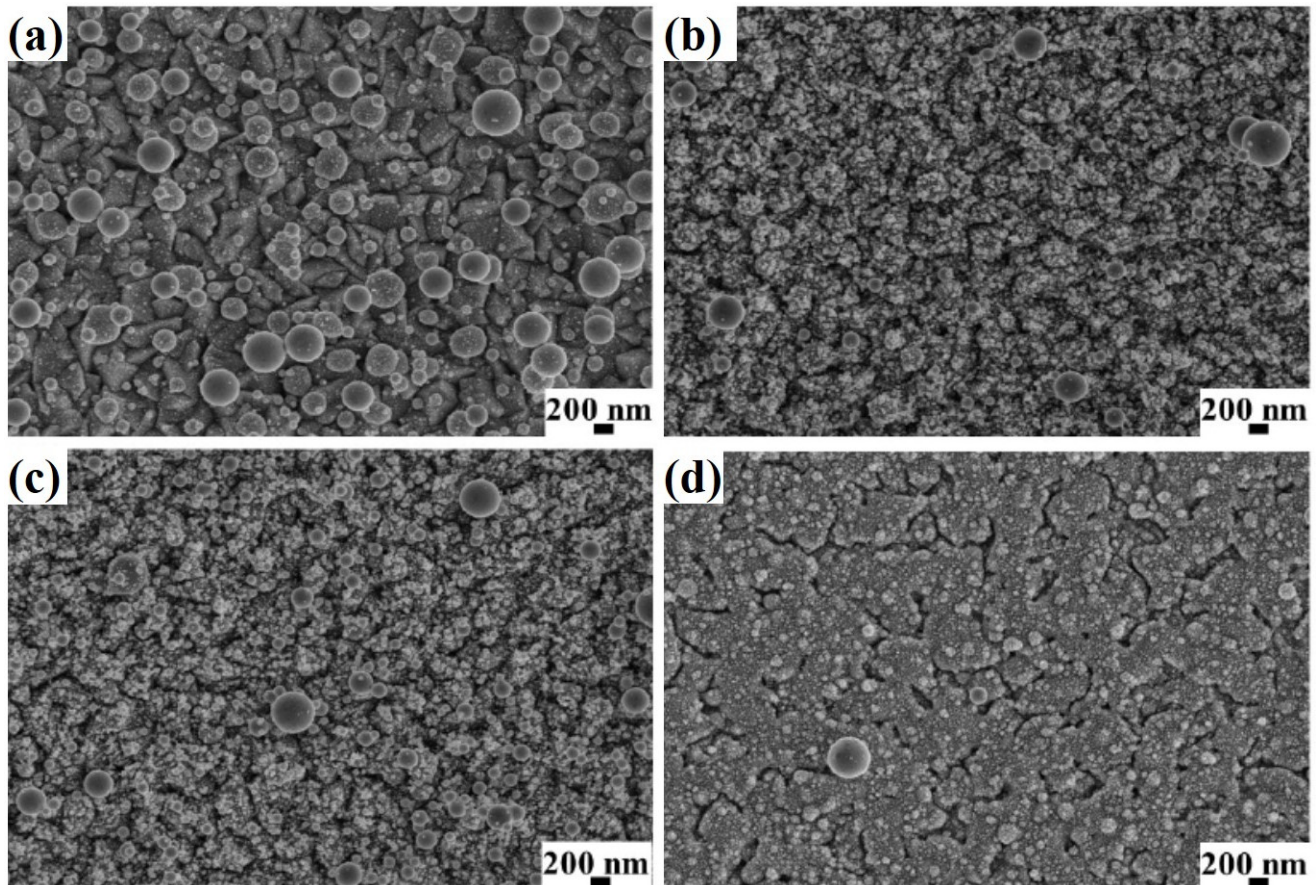


**Figure 3.** SEM images of FTO surface covered by 48.6-nm-thick Au-Pd film and laser irradiated at the fluence values (a)  $0.50 \text{ J/cm}^2$ , (b)  $0.75 \text{ J/cm}^2$ , (c)  $1.00 \text{ J/cm}^2$  and (d)  $1.50 \text{ J/cm}^2$ .

However, by increasing the laser fluence at  $0.75 \text{ J/cm}^2$  (and higher,  $1.0$  and  $1.5 \text{ J/cm}^2$ ) the situation changed: we obtained smaller particles with a lower surface-to-surface distance (higher droplets surface density). Increasing the laser fluence from  $0.75 \text{ J/cm}^2$  to  $1.50 \text{ J/cm}^2$ , the obtained droplets decreased their size, increased their surface density and decreased their surface-to-surface distance. This phenomenon is due to vaporization and re-condensation processes of the de-wetted particles when produced at high laser fluences for which the temperature reached was higher than the material boiling temperature (i.e., photo-fragmentation) [24,25]. This fragmentation occurred due to metal atoms which evaporated from large, formed metal clusters. These evaporated atoms re-condensed on the substrate surface, forming smaller clusters. The final result was the formation of droplets surrounded by smaller droplets.

The melting of the thin metal film as resulting from the laser pulse can be described by considering that the total heat  $S$ , per unit area, transferred to the film of thickness  $d$ , treated by one pulse characterized by the time  $\Delta t$  and having a top-hat temporal profile of

$S = I\Delta t(1 - r)[1 - \exp(-\alpha d)]$ , with  $r$  being the reflectivity of the film at the laser wavelength. For bulk Au, the reflection coefficient at a wavelength of 532 nm is about 0.76 and the optical absorption length is  $\alpha^{-1} = 18$  nm. The reflection coefficient  $r$  and, hence, the absorption coefficient, are functions of  $d$ . If heat losses are not considered, then the temperature rise in a thin film of thickness  $d$  is  $\Delta T = S/Cd$  with  $C$  as the heat capacity per unit volume. In the condition  $\alpha d \ll 1$ , then  $S \sim I\Delta t(1 - r)\alpha d$ . Therefore, with the limit of small  $d$  and ignoring heat conduction,  $\Delta T = I\Delta t(1 - r)\alpha d/C$  can be obtained. Therefore, considering, for example, the fluence  $1.00$  J/cm<sup>2</sup>,  $\alpha = 10^6$  cm<sup>-1</sup> and  $C = 2.5$  J/cm<sup>3</sup> K we obtain, without losses,  $\Delta T \approx 4 \times 10^5$  K, and all droplets had to be immediately evaporated at this temperature. Now, the key point is that for thin films, the heat conductance to the substrate cannot be omitted, in particular if the substrate is highly temperature conductive, such as in the case of FTO. This will change the trend to the opposite, and the melting laser fluence will increase with decreasing film thickness. Thus, the fluence required to melt the film will increase with decreasing  $d$ . As an estimation, for example, taking into account losses, with the fluence  $1$  J/cm<sup>2</sup>,  $\alpha = 10^6$  cm<sup>-1</sup> and  $C = 2.5$  J/cm<sup>3</sup> K, we obtain for  $\Delta T$  about 2000 K [26]. However, this temperature rapidly increases when increasing the laser fluence. To describe our experimental data, we also take into account the results arising from the work of Setoura et al. [27]: they laser irradiated Au nanoparticles (NPs) with a 100 nm diameter deposited on a glass substrate. However, they used a 488-nm-wavelength continuous laser and varied the laser power density from  $10^6$  to  $10^7$  Wcm<sup>-2</sup>. Such a power density is similar to that of a typical nanosecond pulsed laser: for example, in our specific case, using a 10 ns laser pulse, the 0.5–1.5 Jcm<sup>-2</sup> range fluence corresponds to  $5 \times 10^7$ – $1.5 \times 10^8$  Wcm<sup>-2</sup>. Analyzing the transformation of a single NP under the laser irradiation versus the laser power density, the authors recognized the NP fragmentation: increasing the power density, the diameter of the starting NP decreased and, correspondently, a higher number of smaller NPs appeared around the initial NP. The authors evaluated an increase in the NP temperature from about 1200 K to about 6000 K by increasing the laser power density from  $10^6$  to  $5 \times 10^6$  Wcm<sup>-2</sup>. Therefore, the NP is easily heated at temperatures higher than the Au boiling temperature. Consequently, the authors explain the Au NPs fragmentation as a result of the photothermal-laser-induced explosive evaporation. These results suggested to us the following qualitative description of the steps occurring in the formation process of our nanostructures: during the laser irradiation of the Pd or Au-Pd film by the nanosecond pulse, the laser energy is absorbed by the film and the laser-generated heat increases the film temperature above the bulk metals' melting temperatures (the melting temperature of Au is 1337.15 K; the melting temperature of Pd is 1825.15 K). The molten metal film de-wets to form the droplets. However, the laser fluences exploited in this work, 0.5–1.5 J/cm<sup>2</sup>, should be high enough to increase the films' temperature above the metals boiling temperatures, as well (the boiling temperature for Au is 2973.15 K and the boiling temperature for Pd is 3200.15 K). This is due to the fact that the air and FTO/glass constituting the media with which metals interact do not dissipate the laser-generated heat from the NPs rapidly enough (although rapidly enough, however, to avoid the complete ablation of the films). Therefore, NPs' photothermal vaporization can occur after melting. The absorbed energy determines the films' boiling, and then a vapor layer of metal is formed due to the vapor pressure of the liquid metal. The amount of metal vapor depends on the vapor pressure at the metal/air interface, which depends on the temperature  $T$  reached by the NPs. After being cooled, some vaporized metal atoms revert to the starting principal particles, while some are condensed into small particles which are re-deposited on the starting principal particles' surface and on the surrounding FTO substrate. However, a fraction of the atoms can definitely be desorbed from the surface. At the highest fluences, the underlying FTO substrate can also be partially melted, as evident, for example, in Figure 3d.

### 3.2. SERS on Pd Nanostructures

Raman spectra were measured on 4-NTP functionalized nanostructured Pd film irradiated with different laser fluence values of 0 J/cm<sup>2</sup>, 0.5 J/cm<sup>2</sup>, 0.75 J/cm<sup>2</sup>, 1 J/cm<sup>2</sup>

and  $1.5 \text{ J/cm}^2$ . The vibrational modes of 4-NTP molecules were observed in the various laser fluence; see Figure 4 left. The vibrational modes located at  $1080 \text{ cm}^{-1}$ ,  $1110 \text{ cm}^{-1}$ ,  $1340 \text{ cm}^{-1}$  and  $1574 \text{ cm}^{-1}$  were assigned to C-H, C-N,  $\text{NO}_2$  and C-C, respectively. The Raman intensity of vibrational modes attributed to 4-NTP was amplified by the localized electrical field enhanced by Pd nanostructures [28]. In fact, a monolayer of 4-NTP was formed on the Pd surface, and 4-NTP molecules bonded towards its sulfur atom with Pd. Many studies have reported the adsorption of thiol molecules on Pd atoms [29,30]. In conclusion, at ambient temperatures, a 4-NTP layer was formed into a surface without any dimerization effect. As the  $\text{NO}_2$  mode is the most intense, it was used for the adjustment with a Lorentzian function to extract the parameters of the Raman lines (amplitude, Raman peak position and full width at half maximum (FWHM)). Each Raman spectrum represented in Figure 4 left was averaged over four positions of the sample surface. Before fitting, a background subtraction and smoothing were performed on the spectra. Figure 4 right shows the variation of the amplitude, the Raman peak and FWHM by varying the laser fluence. The amplitude increased when the laser fluence increased from 0 to  $0.5 \text{ J/cm}^2$ , and then it changed slightly between  $0.5$  and  $1 \text{ J/cm}^2$ . From  $1 \text{ J/cm}^2$  to  $1.5 \text{ J/cm}^2$ , the amplitude dropped drastically. The Raman peak position located around  $1340 \text{ cm}^{-1}$  shifted to the red when the laser fluence varied from 0 to  $0.5 \text{ J/cm}^2$  and  $0.75$  and  $1 \text{ J/cm}^2$ . It was blue shifted between  $0.5 \text{ J/cm}^2$  and  $0.75 \text{ J/cm}^2$ . The FWHM of the Raman line was decreased when the laser fluence varied from 0 and  $0.5 \text{ J/cm}^2$  and  $0.75$  and  $1 \text{ J/cm}^2$ . It increased from  $0.5$  to  $0.75 \text{ J/cm}^2$  and  $1$  to  $1.5 \text{ J/cm}^2$ . The areas irradiated with the laser exhibited an increase in the Raman intensity between  $0.5 \text{ J/cm}^2$  and  $1 \text{ J/cm}^2$ , and this confirms how the laser affected the optical enhancement of the Pd nanostructures in this range. After exceeding this range, the enhancement decreased drastically due to a change in the morphology of Pd nanostructures. Indeed, with the high laser fluence, the vaporization and re-condensation processes of the de-wetted particles occurred and, hence, a drastic change occurred in the physical properties such as surface density, shape and size, which strongly affect the dielectric function of Pd nanoparticles. The latter deactivates the plasmon mode of Pd nanostructures. The shift of the Raman peak towards the red between 0 and  $0.5 \text{ J/cm}^2$  was due to the film rupture and the formation of nanoparticles; hence, a plasmon resonance of Pd nanostructures could be activated and this led to the fast amplification of SERS, of about three times compared to that without laser fluence [31]. The blue shift between  $0.5$  and  $0.75 \text{ J/cm}^2$  was due to the decrease in the Pd nanostructures' size. It is known that localized surface plasmon resonance (LSPR) shifts towards the short wavelength when the size decreases in the noble metal nanostructures [32,33]. The red shift between  $0.75$  and  $1 \text{ J/cm}^2$  was due to the decreasing and the formation of more spherical particles larger than the case for  $0.75 \text{ J/cm}^2$ . It is clear that the morphology was sufficiently de-wetted and treated by the laser compared to the case of 0 and  $0.5 \text{ J/cm}^2$ ; see Figure 2. It is known that LSPR shifts towards the lower energy when the nanoparticles size increases and the gap distance decreases. However, the fast red shift between 1 and  $1.5 \text{ J/cm}^2$  could be due to the strong modification in the morphology resulting from the higher fluence that caused a vaporization and recondensation. Overall, the laser fluence, FWHM, correlated inversely with the amplitude, e.g., FWHM increased when the amplitude decreased, and inversely. It has been reported that the LSPR band width increases with the increasing of size nanostructures and the decreasing of the gap distance [31]. Indeed, FWHM varies inversely with the variation of LSPR band width. At  $1.5 \text{ J/cm}^2$ , the FWHM increased to around  $70 \text{ cm}^{-1}$ , which reflected an important transition in the structuration and the arrangement of the Pd atomic structure. For example, it is probably that an amorphous phase started forming at this higher laser fluence. The average size calculated from the statistical studies on the samples correlated well with our observation. For example, the two samples irradiated at  $0.75 \text{ J/cm}^2$  and  $1 \text{ J/cm}^2$  had a smaller size and different morphology than  $0 \text{ J/cm}^2$  and  $1.50 \text{ J/cm}^2$ . From the above results, we conclude that a threshold laser fluence is confirmed around  $0.5 \text{ J/cm}^2$ .

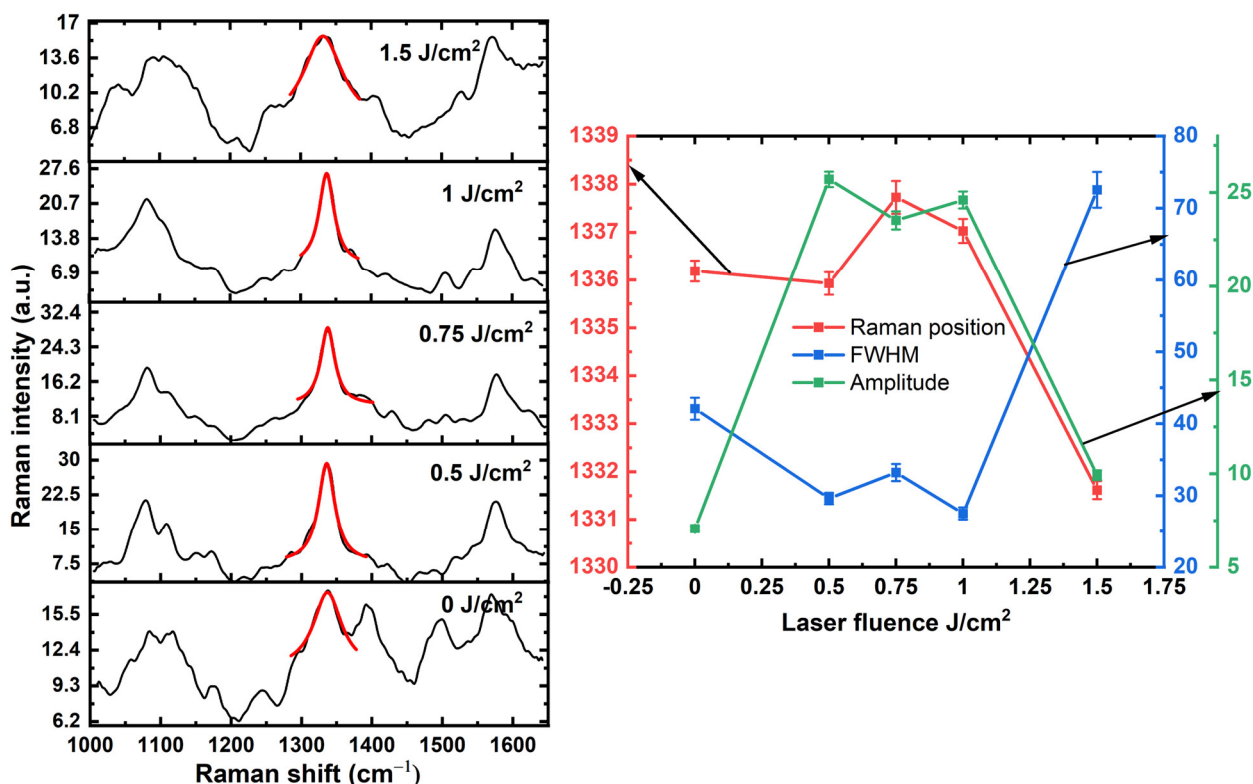


**Figure 4.** On the (left): Raman spectra taken from different areas of Pd with a thickness 17.6 nm irradiated with various laser fluence values (0 J/cm<sup>2</sup>, 0.5 J/cm<sup>2</sup>, 0.75 J/cm<sup>2</sup>, 1 J/cm<sup>2</sup>, 1.5 J/cm<sup>2</sup>), the peak located at 1340 cm<sup>-1</sup> adjusted with a Lorentzian function (red curve); on the (right): extracted parameters (Amplitude, Raman peak position, FWHM) from the adjustment with the Lorentzian function versus laser fluence.

### 3.3. SERS on Au-Pd Nanostructures

Raman spectra were measured on 4-NTP functionalized nanostructured Au-Pd film irradiated with different laser fluence values of 0 J/cm<sup>2</sup>, 0.5 J/cm<sup>2</sup>, 0.75 J/cm<sup>2</sup>, 1 J/cm<sup>2</sup> and 1.5 J/cm<sup>2</sup>. The vibrational modes of 4-NTP molecules were observed at the various laser fluence values; see Figure 5 left. The vibrational modes located at 1080 cm<sup>-1</sup>, 1110 cm<sup>-1</sup>, 1340 cm<sup>-1</sup> and 1574 cm<sup>-1</sup> were assigned to C-H, C-N, NO<sub>2</sub> and C-C, respectively [34]. The Raman intensity of vibrational modes attributed to 4-NTP was amplified by the localized electrical field enhanced by Au-Pd nanostructures [1]. In fact, a monolayer of 4-NTP was formed on the Au-Pd surface and the 4-NTP molecules bonded towards its sulfur atom with Au-Pd. The latter has been reported in different studies [35,36]. In conclusion, at ambient temperatures, a 4-NTP layer is formed into the surface without any dimerization effect. SERS spectra confirmed the non-presence of the dimerization process. As the NO<sub>2</sub> mode is the most intense, it was used for adjustments with a Lorentzian function to extract the parameters of the Raman lines (amplitude, Raman peak position and full width at half maximum (FWHM)). Each Raman spectrum represented in Figure 5 left was averaged over four positions of the sample surface. Figure 5 right shows the variation of the amplitude, the Raman peak and FWHM by varying the laser fluence. We can see that the amplitude increased when the laser fluence increased from 0 to 0.75 J/cm<sup>2</sup>. Then, it decreased from 0.75 to 1.5 J/cm<sup>2</sup>. The Raman peak position located around 1340 cm<sup>-1</sup> shifted to the blue when the laser fluence increased from 0 to 0.5 J/cm<sup>2</sup> and 0.75 and 1.5 J/cm<sup>2</sup>. It was red shifted between 0.5 J/cm<sup>2</sup> and 0.75 J/cm<sup>2</sup>. The FWHM of the Raman line decreased when the laser fluence varied from 0 to 0.5 J/cm<sup>2</sup> and 0.75 and 1 J/cm<sup>2</sup>. It increased slightly from 0.5 to 0.75 J/cm<sup>2</sup> and from 1 to 1.5 J/cm<sup>2</sup>.

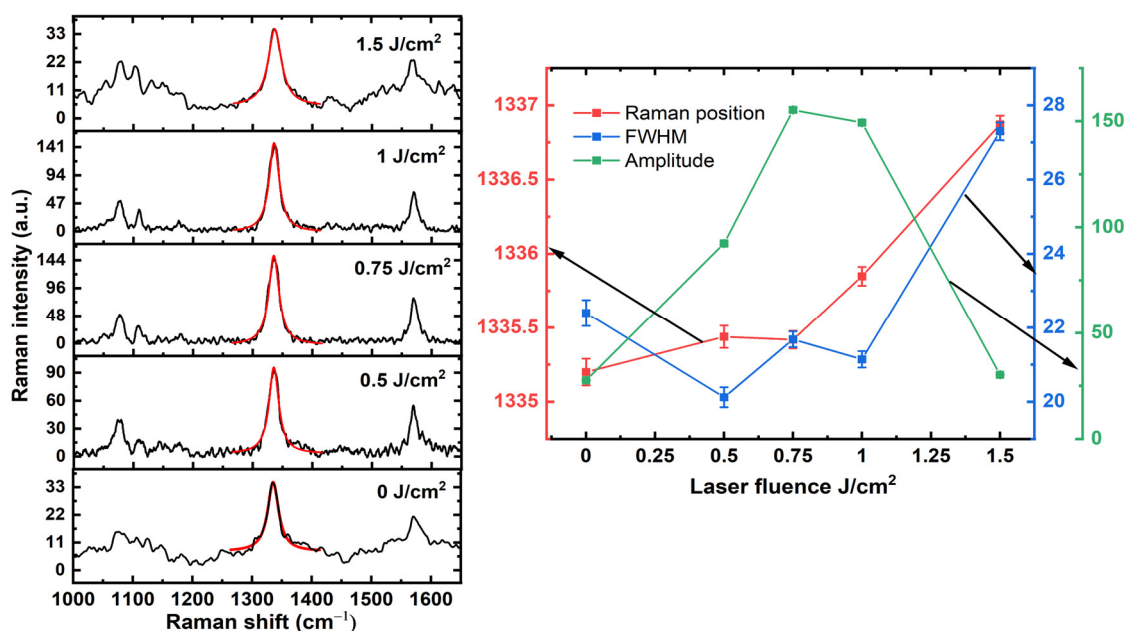


**Figure 5.** On the (left): Raman spectra taken from different areas of Au-Pd with a thickness 48.6 nm irradiated with various laser fluence values (0 J/cm<sup>2</sup>, 0.5 J/cm<sup>2</sup>, 0.75 J/cm<sup>2</sup>, 1 J/cm<sup>2</sup> and 1.5 J/cm<sup>2</sup>), and the peak located at 1340 cm<sup>-1</sup> adjusted with a Lorentzian function (red curve); on the (right): extracted parameters (Amplitude, Raman peak position, FWHM) from the adjustment with the Lorentzian function versus laser fluence.

The areas irradiated with the laser exhibited an increase in the Raman intensity between 0.75 J/cm<sup>2</sup> and 1 J/cm<sup>2</sup>; this confirms how the laser affected the optical enhancement of the Au-Pd nanostructures in this range. After exceeding this range, the enhancement decreased drastically due to a change in the morphology of Au-Pd nanostructures. This is clear in their morphology, as shown in Figure 3d. The shift of the Raman peak towards the blue between 0 and 0.5 J/cm<sup>2</sup> could be due to the transition of the morphology from the semi-continuous film to a nanostructured film with large nanostructures of Au-Pd (see Figure 3); it can clearly be seen that the laser affected the structure of Au-Pd nanostructures, and different studies have reported that there are different LSPR in Au-Pd depending on the arrangement of atoms. We supposed that the LSPR is blue-shifted relative to the excitation wavelength [2,37]. However, the red shift of the Raman peak can be explained by the combination of two effects with the predominance of the gap effect, the decrease in size of the Au-Pd nanoparticles and the decrease in the gap distance between 0.5 and 0.75 J/cm<sup>2</sup>. The blue shift between 0.75 and 1 J/cm<sup>2</sup> could be due to the increase in gap distance accompanying the decrease of optical enhancement. The significant blue shift between 1 and 1.5 J/cm<sup>2</sup> could be due to the transition, again to the photothermal vaporization phenomenon that led to a partial melting of FTO with the metal nanoparticles; see Figure 3d. Overall, the laser fluence for Au-Ag, FWHM correlated inversely with the amplitude between 0 and 0.5 J/cm<sup>2</sup> and between 1 and 1.5 J/cm<sup>2</sup>, e.g., FWHM increased when the amplitude decreased, and inversely. For the range [0.5–1 J/cm<sup>2</sup>], FWHM correlated well with the amplitudes, but it was different in the case of pure Pd. It is known that the LSPR band width increases with the size of nanostructures [1,2]. The average size calculated from the statistical studies on the samples correlates well with our observation. For example, the two samples irradiated at 0 J/cm<sup>2</sup> and 0.75 J/cm<sup>2</sup> have smaller sizes than 0.5 J/cm<sup>2</sup> and 1 J/cm<sup>2</sup>. From the above results, we conclude that a threshold laser fluence is confirmed around 0.75 J/cm<sup>2</sup>.

### 3.4. Effect of Composition

Figure S1 (see Supplementary Materials) shows the variation in amplitude generated by Pd and Au-Pd versus the laser fluence (0 J/cm<sup>2</sup>, 0.5 J/cm<sup>2</sup>, 0.75 J/cm<sup>2</sup>, 1 J/cm<sup>2</sup> and 1.5 J/cm<sup>2</sup>). The maximum optical enhancement was measured at 0.5 J/cm<sup>2</sup> for Pd; however, for Au-Pd it was located at 0.75 J/cm<sup>2</sup>. Au-Pd alloys support the laser fluence more due to its stability. Concerning the variation, it is almost the same for Pd and Au-Pd; overall, Au-Pd showed a high enhancement than pure Pd. This is expected, as the LSPR of Au-Pd is energetically closer to the excitation wavelength than pure Pd [2]. Figure S1 shows the variation in the Raman peak position generated by Pd and Au-Pd versus the laser fluence (0 J/cm<sup>2</sup>, 0.5 J/cm<sup>2</sup>, 0.75 J/cm<sup>2</sup>, 1 J/cm<sup>2</sup> and 1.5 J/cm<sup>2</sup>). The first observation is that the two samples exhibit reverse features in the shift of Raman peak, e.g., when Raman peak shifts to red in Pd, it shifts to blue in Au-Pd, and inversely. This shows that the composition effect strongly affected the plasmon properties of nanostructures that, in turn, affected the Raman shift; it is more composition-dependent than other factors [3,6,38]. Another important point is that the shift variation is more important in the case of Pd than Au-Pd. This confirms the stability of Au-Pd alloys regarding the pure Pd. Figure S1 shows the variation in FWHM generated by Pd and Au-Pd versus the laser fluence (0 J/cm<sup>2</sup>, 0.5 J/cm<sup>2</sup>, 0.75 J/cm<sup>2</sup>, 1 J/cm<sup>2</sup> and 1.5 J/cm<sup>2</sup>). Both Pd and Au-Pd showed similar features; however, the variation was higher in Pd than in Au-Pd. It was experimentally observed that the FWHM of bulk plasmon in pure Pd was larger than in pure Au [2,3,39]. This confirms how alloying increased the resistance of materials and, hence, decreased the change in plasmonic properties. The higher peak position and larger FWHM observed in Pd than Au-Pd correlates well with the position of maximum LSPR and its band width.

### 3.5. Enhancement Estimation and Comparison

The SERS enhancement factor  $G$  is calculated by:

$$G = \frac{I_{SERS}}{I_{Raman}} \frac{N_{Raman}}{N_{SERS}} \quad (1)$$

with  $I_{SERS}$  as the intensity of SERS generated by 4-NTP on Pd and Au-Pd nanoparticles, and  $I_{Raman}$  as the intensity of the Raman far field generated from the SERS substrate where there is no enhancement.  $N_{Raman}$  number of molecules are excited by a laser spot with a diameter of 1.5  $\mu\text{m}$ .  $N_{SERS}$  is the number of molecules excited by the hotspot between the nanoparticles. As the occupied surface area of a molecule is 0.5 nm<sup>2</sup> and the surface of a laser spot is around 1.8  $\mu\text{m}^2$ ,  $N_{Raman}$  is estimated to be approximately 10<sup>6</sup> molecules. It is important to mention that the number of hotspots excited by the gaps  $N$  is much less than  $N$ . The latter depends on the surface density of the nanoparticles, and also on the density of hotspots, based on different statistical studies performed on the hotspots' density reported in our previous work [40]. If we roughly estimate a number of 10<sup>2</sup>–10<sup>3</sup> excited molecules, thus  $\frac{N_{Raman}}{N_{SERS}} = 10^3 - 10^4$ . Based on that, the enhancement factor at 632.8 nm for the Pd and Au-Pd are presented in Table 1. The obtained values are comparable to those reported in the literature, e.g., an enhancement of porous silicon plated palladium nanoparticles was estimated to be 10<sup>5</sup> [41]. Seto et al. reported an enhancement of 10<sup>4</sup>–10<sup>7</sup> for Au-Pd films fabricated with DC magnetron sputtering [42]. Hu et al. developed Au@Pd core-shell nanoparticles with an SERS enhancement factor of 10<sup>3</sup> [43].

**Table 1.** Experimental values of enhancement factor for Pd and Au-Pd with different laser fluence values (0 J/cm<sup>2</sup>, 0.5 J/cm<sup>2</sup>, 0.75 J/cm<sup>2</sup>, 1 J/cm<sup>2</sup> and 1.5 J/cm<sup>2</sup>).

Sample	Enhancement Factor G				
	0 J/cm <sup>2</sup>	0.5 J/cm <sup>2</sup>	0.75 J/cm <sup>2</sup>	1 J/cm <sup>2</sup>	1.5 J/cm <sup>2</sup>
Pd	10 <sup>3</sup> –10 <sup>4</sup>	5 × (10 <sup>3</sup> –10 <sup>4</sup> )	5 × (10 <sup>3</sup> –10 <sup>4</sup> )	5 × (10 <sup>3</sup> –10 <sup>4</sup> )	2 × (10 <sup>3</sup> –10 <sup>4</sup> )
Au-Pd	5 × (10 <sup>3</sup> –10 <sup>4</sup> )	2 × (10 <sup>4</sup> –10 <sup>5</sup> )	3 × (10 <sup>4</sup> –10 <sup>5</sup> )	3 × (10 <sup>4</sup> –10 <sup>5</sup> )	5 × (10 <sup>3</sup> –10 <sup>4</sup> )

#### 4. Conclusions

In this work, we reported an SERS analysis for monometallic Pd and bimetallic Au-Pd nanostructures produced on an FTO surface by laser-induced de-wetting of the deposited Pd or Au-Pd films. In particular, the nanostructuring of the films as induced by the laser irradiations, leading to the formation of nano-droplets from the continuous deposited films, resulted in the increasing of the SERS enhancement factor with respect to the as-deposited untreated film. However, the value of the enhancement factor was strongly dependent on the morphology of the metallic droplets resulting from the laser irradiations. The increase in the laser fluence from 0.5 to 1.5 J/cm<sup>2</sup> resulted in the increase of the droplets' temperature above the Au and Pd boiling temperatures (just at 0.75 J/cm<sup>2</sup>). Hence, at 0.50 J/cm<sup>2</sup> the formation of large, well-separated spherical particles was obtained. At 0.75, 1.00 and 1.50 J/cm<sup>2</sup>, the vaporization process of the de-wetted particles resulted in smaller particles with higher surface density and very close together. This evolution resulted in a decrease in the SERS enhancement factor. The starting deposition thickness of the film (17.6 nm for the pure Pd film and 48.6 nm for the bimetallic Au-Pd film) influenced the sensing property of SERS by establishing different sizes and spacings between the formed nanostructures. Such a connection between morphology and the SERS enhancement factor allows morphology selection on the basis of the fabrication process parameters in order to design materials with desired enhancement factors for desired applications.

**Supplementary Materials:** The following supporting information can be downloaded at: <https://www.mdpi.com/article/10.3390/coatings13040797/s1>, Figure S1: (a) Variation of amplitude as function of the laser fluence for Pd and Au-Pd, (b) Raman peak position, and (c) FWHM.

**Author Contributions:** Conceptualization, C.A. and F.R.; methodology, C.A. and F.R.; formal analysis, C.A. and F.R.; investigation, C.A. and F.R.; resources, C.A. and F.R.; data curation, C.A. and F.R.; writing—original draft preparation, C.A. and F.R.; writing—review and editing, C.A. and F.R. All authors have read and agreed to the published version of the manuscript.

**Funding:** The authors extend their appreciation to the Deputyship for Research and Innovation, Ministry of Education in Saudi Arabia for funding this research work through the project number INST152.

**Institutional Review Board Statement:** Not applicable.

**Informed Consent Statement:** Not applicable.

**Data Availability Statement:** Data sharing is not applicable to this article.

**Acknowledgments:** The authors extend their appreciation to the Deputyship for Research and Innovation, Ministry of Education in Saudi Arabia for funding this research work through the project number INST152.

**Conflicts of Interest:** The authors declare no conflict of interest.

#### References

1. Pergolese, B.; Bigotto, A.; Muniz-Miranda, M.; Sbrana, G. Gold/Palladium and Silver/Palladium Colloids as Novel Metallic Substrates for Surface-Enhanced Raman Scattering. *Appl. Spectrosc.* **2005**, *59*, 194–199. [[CrossRef](#)] [[PubMed](#)]
2. Coviello, V.; Forrer, D.; Amendola, V. Recent Developments in Plasmonic Alloy Nanoparticles: Synthesis, Modelling, Properties and Applications. *ChemPhysChem* **2022**, *23*, e202200136. [[CrossRef](#)] [[PubMed](#)]
3. Toshima, N.; Yonezawa, T. Bimetallic nanoparticles—Novel materials for chemical and physical applications. *New J. Chem.* **1998**, *22*, 1179–1201. [[CrossRef](#)]
4. Li, Z.; Wang, R.; Kurouski, D. Nanoscale Photocatalytic Activity of Gold and Gold–Palladium Nanostructures Revealed by Tip-Enhanced Raman Spectroscopy. *J. Phys. Chem. Lett.* **2020**, *11*, 5531–5537. [[CrossRef](#)] [[PubMed](#)]
5. Jiang, T.; Jia, C.; Zhang, L.; He, S.; Sang, Y.; Li, H.; Li, Y.; Xu, X.; Liu, H. Gold and gold–palladium alloy nanoparticles on heterostructured TiO<sub>2</sub> nanobelts as plasmonic photocatalysts for benzyl alcohol oxidation. *Nanoscale* **2015**, *7*, 209–217. [[CrossRef](#)]
6. Boltersdorf, J.; Leff, A.C.; Forcherio, G.T.; Baker, D.R. Plasmonic Au–Pd Bimetallic Nanocatalysts for Hot-Carrier-Enhanced Photocatalytic and Electrochemical Ethanol Oxidation. *Crystals* **2021**, *11*, 226. [[CrossRef](#)]
7. Hu, J.-W.; Li, J.-F.; Ren, B.; Wu, D.-Y.; Sun, S.-G.; Tian, Z.-Q. Palladium-Coated Gold Nanoparticles with a Controlled Shell Thickness Used as Surface-Enhanced Raman Scattering Substrate. *J. Phys. Chem. C* **2007**, *111*, 1105–1112. [[CrossRef](#)]

8. Liu, W.; Zheng, G.; Wong, W.-L.; Wong, K.-Y. Au-Pd alloy nanoparticles catalyze the colorimetric detection of hydrazine with methylene blue. *Inorg. Chem. Commun.* **2019**, *107*, 107455. [CrossRef]
9. Scott, R.W.J.; Wilson, O.M.; Oh, S.-K.; Kenik, E.A.; Crooks, R.M. Bimetallic Palladium–Gold Dendrimer-Encapsulated Catalysts. *J. Am. Chem. Soc.* **2004**, *126*, 15583–15591. [CrossRef]
10. El-Khoury, P.Z.; Gong, Y.; Abellan, P.; Arey, B.W.; Joly, A.G.; Hu, D.H.; Evans, J.E.; Browning, N.D.; Hess, W.P. Tip-Enhanced Raman Nanographs: Mapping Topography and Local Electric Fields. *Nano Lett.* **2015**, *15*, 2385–2390. [CrossRef]
11. Huang, Y.-F.; Wu, D.-Y.; Zhu, H.-P.; Zhao, L.-B.; Liu, G.-K.; Ren, B.; Tian, Z.-Q. Surface-enhanced Raman spectroscopic study of p-aminothiophenol. *Phys. Chem. Chem. Phys.* **2012**, *14*, 8485–8497. [CrossRef]
12. Park, C.G.; Kim, J.Y.; Lee, E.; Choi, H.K.; Park, W.H.; Kim, J.; Kim, Z.H. Tip-Enhanced Raman Scattering with a Nanoparticle-Functionalized Probe. *Bull. Korean Chem. Soc.* **2012**, *33*, 1748–1752. [CrossRef]
13. Awada, C.; Dab, C.; Grimaldi, M.G.; Alshoaibi, A.; Ruffino, F. High optical enhancement in Au/Ag alloys and porous Au using Surface-Enhanced Raman spectroscopy technique. *Sci. Rep.* **2021**, *11*, 4714. [CrossRef] [PubMed]
14. Ding, J.; Li, X.; Chen, L.; Zhang, X.; Sun, S.; Bao, J.; Gao, C.; Tian, X. Au–Pt alloy nanoparticles site-selectively deposited on CaIn<sub>2</sub>S<sub>4</sub> nanosteps as efficient photocatalysts for hydrogen production. *J. Mater. Chem. A* **2016**, *4*, 12630–12637. [CrossRef]
15. Li, X.; Odoom-Wubah, T.; Huang, J. Biosynthesis of Ag–Pd bimetallic alloy nanoparticles through hydrolysis of cellulose triggered by silver sulfate. *RSC Adv.* **2018**, *8*, 30340–30345. [CrossRef]
16. Kunal, P.; Li, H.; Dewing, B.L.; Zhang, L.; Jarvis, K.; Henkelman, G.; Humphrey, S.M. Microwave-Assisted Synthesis of Pd<sub>x</sub>Au<sub>100-x</sub> Alloy Nanoparticles: A Combined Experimental and Theoretical Assessment of Synthetic and Compositional Effects upon Catalytic Reactivity. *ACS Catal.* **2016**, *6*, 4882–4893. [CrossRef]
17. Shubin, Y.; Plyusnin, P.; Sharafutdinov, M. In situ synchrotron study of Au–Pd nanoporous alloy formation by single-source precursor thermolysis. *Nanotechnology* **2012**, *23*, 405302. [CrossRef]
18. De, G.; Rao, C.N.R. Au–Pt alloy nanocrystals incorporated in silica films. *J. Mater. Chem.* **2005**, *15*, 891–894. [CrossRef]
19. Available online: <http://www.kintec.hk/> (accessed on 12 March 2023).
20. Torrisi, V.; Censabella, M.; Piccitto, G.; Compagnini, G.; Grimaldi, M.G.; Ruffino, F. Characteristics of Pd and Pt Nanoparticles Produced by Nanosecond Laser Irradiations of Thin Films Deposited on Topographically-Structured Transparent Conductive Oxides. *Coatings* **2019**, *9*, 68. [CrossRef]
21. Ruffino, F.; Pugliara, A.; Carria, E.; Bongiorno, C.; Spinella, C.; Grimaldi, M.G. Formation of nanoparticles from laser irradiated Au thin film on SiO<sub>2</sub>/Si: Elucidating the Rayleigh-instability role. *Mater. Lett.* **2012**, *84*, 27–30. [CrossRef]
22. Wang, J.T.; Shi, X.L.; Zhong, X.H.; Wang, J.N.; Pyrah, L.; Sanderson, K.D.; Ramsey, P.M.; Hirata, M.; Tsuru, K. Morphology control of fluorine-doped tin oxide thin films for enhanced light trapping. *Sol. Energy Mater. Sol. Cells* **2015**, *132*, 578–588. [CrossRef]
23. Gentile, A.; Cacciato, G.; Ruffino, F.; Reitano, R.; Scapellato, G.; Zimbone, M.; Lombardo, M.; Battaglia, A.; Gerardi, C.; Foti, M.; et al. Nanoscale structuration and optical properties of thin gold films on textured FTO. *J. Mater. Sci.* **2014**, *49*, 8498–8507. [CrossRef]
24. Henley, S.J.; Carrey, J.D.; Silva, S.R.P. Pulsed-laser-induced nanoscale island formation in thin metal-on-oxide films. *Phys. Rev. B* **2005**, *72*, 195408. [CrossRef]
25. Ruffino, F.; Maugeri, P.; Cacciato, G.; Zimbone, M.; Grimaldi, M.G. Metal nanostructures with complex surface morphology: The case of supported lumpy Pd and Pt nanoparticles produced by laser processing of metal films. *Phys. E* **2016**, *83*, 215–226. [CrossRef]
26. Ruffino, F.; Carria, E.; Kimiagar, S.; Crupi, I.; Simone, F.; Grimaldi, M.G. Formation and Evolution of Nanoscale Metal Structures on ITO Surface by Nanosecond Laser Irradiations of Thin Au and Ag Films. *Sci. Adv. Mater.* **2012**, *4*, 708–718. [CrossRef]
27. Setoura, K.; Okada, Y.; Hashimoto, S. CW-laser-induced morphological changes of a single gold nanoparticle on glass: Observation of surface evaporation. *Phys. Chem. Chem. Phys.* **2014**, *16*, 26938–26945. [CrossRef]
28. Bai, Y.; Feng, F.; Zhao, L.; Wang, C.; Wang, H.; Tian, M.; Qin, J.; Duan, Y.; He, X. Aptamer/thrombin/apptamer-AuNPs sandwich enhanced surface plasmon resonance sensor for the detection of subnanomolar thrombin. *Biosens. Bioelectron.* **2013**, *47*, 265–270. [CrossRef]
29. Rogers, S.M.; Dimitratos, N.; Jones, W.; Bowker, M.; Kanaras, A.G.; Wells, P.P.; Catlow, C.R.A.; Parker, S.F. The adsorbed state of a thiol on palladium nanoparticles. *Phys. Chem. Chem. Phys.* **2016**, *18*, 17265–17271. [CrossRef]
30. Carro, P.; Corthey, G.; Rubert, A.A.; Benitez, G.A.; Fonticelli, M.H.; Salvarezza, R.C. The Complex Thiol–Palladium Interface: A Theoretical and Experimental Study. *Langmuir* **2010**, *26*, 14655–14662. [CrossRef]
31. Ruan, F.; Zhang, S.; Li, Z.; Yang, Z.; Wu, D.; Ren, B.; Xu, H. Near-field coupling and SERS effects of palladium nanoparticle dimers. *Chin. Sci. Bull.* **2010**, *55*, 2930–2936. [CrossRef]
32. Olk, P.; Renger, J.; Wenzel, M.T.; Eng, L.M. Distance Dependent Spectral Tuning of Two Coupled Metal Nanoparticles. *Nano Lett.* **2008**, *8*, 1174–1178. [CrossRef] [PubMed]
33. Awada, C.; Hajlaoui, T.; Al Suliman, N.; Dab, C. Heterogeneous Nanoplasmonic Amplifiers for Photocatalysis—Application: A Theoretical Study. *Catalysts* **2022**, *12*, 771. [CrossRef]
34. Juergensen, S.; Kusch, P.; Reich, S. Resonant Raman Scattering of 4-Nitrothiophenol. *Phys. Status Solidi* **2020**, *257*, 2000295. [CrossRef]
35. Awada, C.; Abdullah, M.M.B.; Traboulsi, H.; Dab, C.; Alshoaibi, A. SARS-CoV-2 Receptor Binding Domain as a Stable-Potential Target for SARS-CoV-2 Detection by Surface-Enhanced Raman Spectroscopy. *Sensors* **2021**, *21*, 4617. [CrossRef] [PubMed]

36. Dab, C.; Awada, C.; Merlen, A.; Ruediger, A. Near-field chemical mapping of gold nanostructures using a functionalized scanning probe. *Phys. Chem. Chem. Phys.* **2017**, *19*, 31063–31071. [[CrossRef](#)]
37. Danielis, N.; Vega, L.; Fronzoni, G.; Stener, M.; Bruix, A.; Neyman, K.M. AgPd, AuPd, and AuPt Nanoalloys with Ag- or Au-Rich Compositions: Modeling Chemical Ordering and Optical Properties. *J. Phys. Chem. C* **2021**, *125*, 17372–17384. [[CrossRef](#)]
38. Nikov, R.G.; Nedyalkov, N.N.; Dikovska, A.O.; Karashanova, D.B. Nanonetworks fabrication by laser ablation in water of bimetallic compositions of platinum and palladium with gold and silver. *Lasers Manuf. Mater. Process.* **2022**, *9*, 102–116. [[CrossRef](#)]
39. Lee, K.E.; Shivhare, A.; Hu, Y.; Scott, R.W.J. Supported bimetallic AuPd clusters using activated Au<sub>25</sub> clusters. *Catal. Today* **2017**, *280*, 259–265. [[CrossRef](#)]
40. Awada, C.; Plathier, J.; Dab, C.; Charra, F.; Douillard, L.; Ruediger, A. High resolution scanning near field mapping of enhancement on SERS substrates: Comparison with photoemission electron microscopy. *Phys. Chem. Chem. Phys.* **2016**, *18*, 9405–9411. [[CrossRef](#)]
41. Al-Syadi, A.M.; Faisal, M.; Harraz, F.A.; Jalalah, M.; Alsaiani, M. Immersion-plated palladium nanoparticles onto meso-porous silicon layer as novel SERS substrate for sensitive detection of imidacloprid pesticide. *Sci. Rep.* **2021**, *11*, 9174. [[CrossRef](#)]
42. Abd El-Aal, M.; Seto, T. Surface-enhanced Raman scattering and catalytic activity studies over nanostructured Au–Pd alloy films prepared by DC magnetron sputtering. *Res. Chem. Intermed.* **2020**, *46*, 3741–3756. [[CrossRef](#)]
43. Hu, J.-W.; Zhang, Y.; Li, J.-F.; Liu, Z.; Ren, B.; Sun, S.-G.; Tian, Z.-Q.; Lian, T. Synthesis of Au@Pd core–shell nanoparticles with controllable size and their application in surface-enhanced Raman spectroscopy. *Chem. Phys. Lett.* **2005**, *408*, 354–359. [[CrossRef](#)]

**Disclaimer/Publisher’s Note:** The statements, opinions and data contained in all publications are solely those of the individual author(s) and contributor(s) and not of MDPI and/or the editor(s). MDPI and/or the editor(s) disclaim responsibility for any injury to people or property resulting from any ideas, methods, instructions or products referred to in the content.